1   **The RNA helicase DDX5 promotes alveolar rhabdomyosarcoma growth**
2   **and survival**
3

4   Alberto Gualtieri[1], Valerio Licursi[2] and Chiara Mozzetta[1][#].

5

6   1. Institute of Molecular Biology and Pathology (IBPM), National Research Council (CNR)

7   of Italy c/o Department of Biology and Biotechnology "C. Darwin", Sapienza University,

8   00185 Rome, Italy

9   2. Department of Biology and Biotechnology "C. Darwin", Sapienza University, 00185

10 Rome, Italy

11

12 #Correspondence: chiara.mozzetta@uniroma1.it (C.M)

13

14   **Abstract**

15   Rhabdomyosarcoma (RMS) is the most common soft-tissue sarcoma of childhood

16   characterized by the inability to exit the proliferative myoblast-like stage. The alveolar

17   fusion positive subtype (FP-ARMS) is the most aggressive and is mainly caused by the

18   expression of PAX3/7-FOXO1 oncoproteins, which are challenging pharmacological

19   targets. Thus, other therapeutic vulnerabilities resulting from gene expression changes

20   are progressively being recognized. Here, we identified the DEAD box RNA helicase 5

21   (DDX5) as a potential therapeutic target to inhibit FP-ARMS growth. We show that DDX5

22   is overexpressed in alveolar RMS cells, demonstrating that its depletion drastically

23   decreases FP-ARMS viability and slows tumor growth in xenograft models.

24   Mechanistically, we provide evidence that DDX5 functions upstream the G9a/AKT

25   survival signalling pathway, by modulating G9a protein stability. Finally, we show that

26   G9a interacts with PAX3-FOXO1 and regulates its activity, thus sustaining FP-ARMS

27   myoblastic state. Together, our findings identify a novel survival-promoting loop in FP-

28   ARMS and highlight DDX5 as potential therapeutic target to arrest rhabdomyosarcoma

29   growth.

30

31   **Keywords**

32   Rhabdomyosarcoma, DDX5, PAX3-FOXO1, tumor growth, G9a.

33

34

35

36

37

38

39

40

Introduction

Rhabdomyosarcomas (RMS) are aggressive childhood cancers representing the most common soft-tissue sarcomas in pediatric population. Around 60% of all children and adolescents diagnosed with RMS are cured by currently available multimodal therapies, including surgery, radiation and conventional chemotherapeutic drugs. However, clinical outcomes for patients with high-risk RMS are still poor, emphasizing the urgency to explore more in depth its molecular underpinnings and to devise new effective therapeutic interventions (1).

Pediatric RMS are typically divided into two major categories: alveolar (ARMS) and embryonal (ERMS). These two types of RMS are clinically and molecularly different. ERMS are more common, histologically resemble embryonic skeletal muscle, arise early in childhood from head, neck and retroperitoneum, and are typically associated with better prognosis. The genetic profile of ERMS is heterogeneous and is associated with activation of various tumor-promoting signaling pathways and/or loss of tumor surveillance. ARMS are most common in older children, predominantly involve trunk and extremities and are generally more aggressive. They typically associate with pathognomonic chromosomal translocations, such as t(2;13) or t(1;13) that result in fusion proteins combining the DNA binding domain of PAX3 or PAX7 with the transcriptional activation domain of FOXO1A, which account for the 60% or 20% ARMS cases, respectively. The remaining 20% of ARMS lack molecular evidence of these translocations and are referred to as fusion-negative ARMS (2).

Alveolar fusion-positive (FP-ARMS) is the most aggressive subtype, associated with frequent metastasis at the time of diagnosis and limited response to treatment, resulting in poor survival rates. FP-RMS cells are addicted to the oncogenic capacity of PAX3/7-FOXO1, which have become very important prognostic markers in the clinics. However, direct targeting of the fusion proteins is still a challenge (3) and other therapeutic vulnerabilities resulting from gene expression changes are being extensively

3

68   investigated in the last years (4-7). In this context, DEAD box RNA helicases appear

69   appealing candidates as potential therapeutic targets, having been implicated in almost

70   every aspect of RNA metabolism, including transcription, pre-mRNA splicing, ribosome

71   biogenesis, transport, translation, and RNA decay (8).

72   In normal myogenesis, the DEAD box helicase 5 (DDX5, also known as p68) is needed

73   for proper differentiation, being part of a multitasking complex that together with the

74   steroid nuclear receptor activator (*SRA*) long-non coding RNA, BRG1 and MYOD,

75   promotes transcriptional expression of MYOD-target genes (9). Moreover, DDX5

76   cooperates with heterogeneous nuclear ribonucleoprotein (hnRNP) to establish specific

77   splicing subprograms in myoblasts along myogenesis (10), highlighting its multimodal

78   actions in shaping the gene expression programs during cell differentiation. Many studies

79   have detected the overexpression of DDX5 in different human malignancies and

80   confirmed its involvement in tumorigenesis, invasion, proliferation and metastasis (11-

81   13). Thus, DDX5 is a potentially valuable diagnostic and prognostic marker in cancer.

82   However, whether DDX5 plays a role in rhabdomyosarcoma pathogenesis has been not

83   addressed yet. Here, we demonstrate that DDX5 is overexpressed in FP-ARMS and that

84   it promotes their survival and growth, both *in vitro* and *in vivo*. Mechanistically, we found

85   that DDX5 interacts and cooperates with the lysine methyltransferase G9a to stabilize

86   PAX3-FOXO1 thus sustaining the myoblastic stage of FP-ARMS.

87

4

Results and Discussion

DDX5 is overexpressed in rhabdomyosarcoma and sustains FP-ARMS survival

To gain insights into a possible role of DDX5 in RMS, we looked at its expression and epigenetic status through the Integrated Rhabdomyosarcoma database of the St. Jude Children's Research Hospital (https://pecan.stjude.cloud/proteinpaint/study/RHB2018) (14). Among the 18 chromatin hidden Markov modeling (chromHMM) states (15) identified in the study (14) (**Supplemental Figure. 1A**), DDX5 showed a strong active transcription start site (TSS) (red bars) and an actively transcribed gene body (green bars) in either normal myoblasts and myotubes, and primary ERMS and ARMS samples (**Supplemental Figure 1B**). Accordingly, *DDX5* RNA levels (*DDX5* FPKM) did not significantly differ among normal and RMS samples (**Figure 1A,** *blue bars*). By contrast, proteomic data revealed that DDX5 protein levels were higher than normal cells in all tested RMS samples (**Figure 1A,** *red bars*), which were also accompanied by an hyperphosphorylated status of DDX5 as compared to normal myoblasts (**Figure 1A,** *circles*). Experimental analysis of DDX5 expression, by quantitative real-time PCR (qRT-PCR) (**Figure 1B)** and Western blot (WB) (**Figure 1C**), on two different FP-ARMS cell lines, RH30 and RH41, confirmed DDX5 overexpression in FP-ARMS, as compared to normal <u>h</u>uman <u>s</u>keletal <u>m</u>uscle <u>m</u>yoblasts (HSMMs)**,** prompting our interest in investigating its functional role.

To this end, we inhibited DDX5 expression in FP-ARMS cells through small interfering RNA (siRNA)-mediated knock-down (KD). RH30 and RH41 cells were transfected with two different siRNA against DDX5 or with scramble siRNAs as control (siCTR). As demonstrated by qRT-PCR (**Figure 1D**) and western blot (**Figure 1E**) analysis, both siRNAs efficiently depleted DDX5 in both cell lines. A growth curve performed on both RH30 (**Figure 1F,** *right panel*) and RH41 (**Figure 1F,** *left panel*), demonstrated that DDX5 depletion significantly reduced FP-RMS growth, as compared to control cells

114   (siCTR). An effect that was visible by morphological inspection upon 72 hrs after

115   treatment, (**Figure 1G)**. Western blot analysis for the apoptotic markers cleaved PARP

116   and cleaved caspase 7 (**Figure 1H**), clearly demonstrated the induction of programmed

117   cell death in FP-ARMS upon reduction of DDX5 expression. Taken together, these data

118   led us to conclude that overexpression of DDX5 sustains FP-RMS growth and survival.

119

120   **DDX5 promotes AKT signaling stabilizing G9a in FP-RMS**

121   To gain further insights into the mechanism behind DDX5 role in sustaining FP-RMS

122   survival, we performed transcriptional profiling by RNA-seq in siDDX5 Rh30 cells, as

123   compared to siCTR-transfected cells (**Figure 2A**). Notably, enrichment analysis of the

124   differentially expressed genes (DEGs; *p<0.05, FC>1.5*) found "regulation of RAS protein

125   signal transduction" among categories enriched in down-regulated transcripts (**Figure**

126   **2B**). This evidence caught our attention, as RAS pathway is one of the most de-regulated

127   in both FN-RMS and FP-RMS (16). Its predominant downstream signaling pathways,

128   such as the RAF–MEK (mitogen-activated protein kinase (MAPK) kinase–ERK

129   (extracellular signal–regulated kinase) MAPK pathway and the phosphatidylinositol 3-

130   kinase (PI3-kinase)–AKT–mammalian target of rapamycin (mTOR) pathway), are key to

131   maintain cell growth and proliferation, which is why their inhibition is being tested to arrest

132   cancer cell survival (17), with positive effects reported also in RMS (18). Of note, KEGG

133   analysis of 'RAS signaling' pathway **(Figure 2C,** *left panel***)** indicated that among its

134   downstream cascades, the **'**Akt signaling' pathway was the one affected by DDX5

135   depletion. Accordingly, KEGG on the specific 'PI3K-Akt signaling' pathway highlighted

136   downregulation of *AKT* **(Figure 2C,** *right panel)*. AKT is involved in cell survival and

137   proliferation, through the mTOR pathway (19), and in apoptosis inhibition by blocking the

138   FOXO cascade (20). To validate this finding, we performed qRT-PCR for AKT on RH30

139   cell lines after 3 days siDDX5 treatment, demonstrating a significant reduction of AKT

140   mRNA levels as compared to siCTR cells (**Figure 2D**). Moreover, by western blot

141   analysis we demonstrated that *DDX5* silencing induced a significant reduction of the

142   protein levels of AKT and, consequently, of p-AKT, the fully activated form of the kinase

143   phosphorylated on Thr 308 and Ser 473 (**Figure 2E**)**.** These data agree with recent work

144   demonstrating that DDX5 promotes hepatocellular carcinoma cell growth *via* AKT

145   pathway (21), supporting a similar role for DDX5 in sustaining FP-ARMS growth and

146   survival.

147   It has been recently reported that AKT signaling is also pathogenically activated in FP-

148   ARMS by the lysine methyltransferase G9a (22), an evidence that led us to hypothesize

149   that DDX5 and G9a might exert their function *via* a common regulatory axis on AKT. To

150   investigate for this potential cooperation, we performed co-immunoprecipitation studies

151   in RH41 cells in control condition (shCTR) and in cells depleted of G9a (by short-hairpin

152   RNA against G9a, shG9a). As shown in **Figure 2F**, we demonstrated the presence of

153   DDX5 in the immunoprecipitation of G9a, which was reduced in cells with decreased

154   levels of G9a, confirming the specificity of the interaction (**Figure 2F**). In further support

155   for a possible cooperation between G9a and DDX5, we showed that G9a depletion in

156   FP-ARMS cells phenocopied the downregulation of DDX5. Indeed, shG9a FP-ARMS

157   displayed growth arrest (**Supplemental Figure 2A-B)**; and an increased expression of

158   apoptotic markers (**Supplemental Figure 2C**). Then, to better investigate the

159   relationship between DDX5 and G9a, we studied their reciprocal modulation. While G9a

160   reduction had no effect on DDX5 protein levels (**Figure 2F,** *input lanes*), we observed

161   that depletion of DDX5 led to a significant reduction of G9a protein in RH41 cells (**Figure

162   2G**). Since G9a mRNA levels did not significantly decreased after DDX5 silencing

163   (**Figure 2H**), our results suggest that DDX5 regulates G9a post-transcriptionally. In

164   agreement with this idea, it has been recently demonstrated that DDX5 is involved in the

165   alternative splicing of *G9a* transcripts in spermatogonia (23) a mechanism that has been

166   also shown to affect the stability of different G9a isoforms during neuronal differentiation

167   (24). These results lead to speculate that DDX5 might be involved in the control of *G9a*

168   splicing also in FP-ARMS, likely stabilizing specific isoforms and ultimately affecting G9a

169   protein stability.

170   Taken together, our data indicate that DDX5 function upstream of G9a to promote cell

171   growth and survival, at least in part, via AKT modulation.

172

173   **G9a regulates PAX3-FOXO1 protein stability thus sustaining FP-RMS myoblastic**

174   **state**

175   FP-RMS are addicted to the oncogenic capacity of PAX3-FOXO1, which has been firmly

176   implicated in perpetuating the myoblastic proliferative state of RMS cells (7). In light of

177   our results showing that DDX5 and G9a downregulation disrupt this survival-promoting

178   loop, we decided to investigate whether DDX5 and G9a could be involved in the PAX3-

179   FOXO1 modulation.

180   Of note, depletion of both *DDX5* (**Figure 3A**) and G9a (**Figure 3B**) caused a marked

181   reduction of PAX3-FOXO1 protein; while PAX3-FOXO1 mRNA levels remained

182   unaffected **(Supplemental Figure 3A)**, pointing towards a post-transcriptional

183   regulation. Since PAX3-FOXO1 reduction was observed also upon G9a depletion, a

184   condition in which DDX5 levels are unaffected (**Figure 2F**), we hypothesized that G9a is

185   the major regulator of PAX3-FOXO1 oncoprotein in this axis. In agreement with this idea,

186   inhibition of G9a enzymatic activity by treatment with two specific small molecule

187   inhibitors, A366 (**Figure 3C**) and UNC0642 (**Figure 3D**), exerted similar effects on PAX3-

188   FOXO1 levels, further suggesting that G9a mediates PAX3-FOXO1 stability via its

189   enzymatic activity. Accordingly, we found that G9a interacted with PAX3-FOXO1 in two

190   different FP-RMS cell lines (**Figure 3E**), and this interaction was reduced in cells treated

191   with the G9a inhibitor A-366 (**Figure 3F**). As G9a has a well-known role in methylating

192   non-histone proteins, and lysine methylation promotes protein stability (25), these results

193   strongly suggest that G9a might stabilize PAX3-FOXO1 through methylation. In further

194   support of this, transcriptomic analysis by RNA-seq revealed that G9a depletion in FP-

195   ARMS cells (**Supplemental Figure 3B**) induced transcriptional changes inversely

196   correlated by those imposed by PAX3-FOXO1 expression (26, 27), as revealed by Gene

197   Set Enrichment Analysis (GSEA) (**Figure 3G**). Accordingly, transcript levels of known

198   PAX3-FOXO1 target genes were reduced in G9a KD cells (**Figure 3H**). Further, it has

199   been previously shown that PAX3-FOXO1 activates the RMS master transcription

200   factors (MTFs) MYOD1 and Myogenin, and together with them establishes the

201   epigenome and transcriptional signatures of FP-RMS (7). Strikingly, G9a down-

202   regulation (**Figure 3I,L**) and pharmacological inhibition (**Figure 3M**) was sufficient to

203   induce a strong reduction of MYOD1 and Myogenin expression, both at the RNA (**Figure

204   3I**) and protein (**Figure 3L,M**) levels. This was confirmed by GSEA that revealed a

205   striking negative correlation of transcripts belonging to the "Myogenesis" hallmark in G9a

206   depleted cells (**Supplemental Figure 3C**), as compared to control. Taken together,

207   these evidences strongly indicate that G9a activity promotes the PAX3-FOXO1-induced

208   myoblastic RMS stage stabilizing the stability of the oncoprotein.

209

210   **DDX5 promotes FP-RMS growth *in vivo***

211   Our results identified the existence of a three-component regulation axis in which DDX5

212   functions upstream of G9a and PAX3-FOXO1 to sustain FP-ARMS survival. To

213   unequivocally demonstrate a role of DDX5 in mediating FP-ARMS tumorigenesis *in vivo*,

214   we performed xenografts experiments. To this end, we subcutaneously injected both

215   control (shCtr) and DDX5 depleted RH30 cells (shDDX5) into the flanks of BALB/c Nude

216   mice. Consistent with our *in vitro* data, tumors derived from shDDX5 displayed a

217   significantly reduced growth over time as compared to those derived from control cells

218   (shCtr) (**Figure 4A**); and excised tumors were much smaller than controls (**Figure 4B**).

219   Moreover, immunohistological analysis demonstrated that shDDX5 isolated tumors

220   displayed a significant reduced number of proliferating (Ki67+) cells, as compared to

221   those derived from control (shCtr) cells (**Figure 4C**). These results are consistent with

222   the growth inhibition we previously observed *in vitro* and demonstrate that DDX5 plays

223   a crucial role in FP-RMS growth *in vivo*. Moreover, western blot analysis on xenografts-

224   derived protein extracts confirmed our *in vitro* data, showing a DDX5-dependent

225   expression of G9a and PAX3-FOXO1 in RMS tumors (**Figure 4D-E**), confirming that

226   DDX5 downregulation also reduces pAKT, AKT and MYOD1 protein (**Figure 4E**) levels

227   *in vivo*.

228   In sum, our data identify a major role for DDX5 in sustaining FP-ARMS survival and

229   designate it as a possible novel therapeutic target for rhabdomyosarcoma. DDX5 ha

230

231 **Methods**

232 **Cell lines**

233 All cell lines were maintained in a humidified incubator at 37°C with 5% CO2. Primary

234 human skeletal muscle myoblasts (HSMMs) were cultured in growth medium (SkGM-2

235 Bullet Kit, Lonza). HEK293T cells (kindly gifted by Slimane Ait-Si-Ali lab) for the

236 production of lentiviral particles were cultured in Dulbecco's modified Eagle's medium

237 (DMEM) (Sigma-Aldrich, D5671), supplemented with 10% FBS (Corning, 35-015-CV), 2

238 mM L-glutamine and 100 U/ml penicillin/ streptomycin. ARMS cell lines RH30 and RH41

239 were kindly provided by Rossella Rota (Bambino Gesù Children's Hospital, Rome, Italy).

240 RH30 and RH41 were maintained in RPMI 1640 with L-glutamine (Sigma-Aldrich,

241 R8758,) supplemented with with 1% penicillin/streptomycin and 10% FBS (Corning, 35-

242 015-CV). Cells were treated with 2μM UNC0642 and 10 μM A366 (Sigma-Aldrich,

243 SML1410-25MG) Control cells were treated with equivalent concentrations of DMSO

244 (Sigma-Aldrich). Several first passage aliquots of each cell line were stored in liquid

245 nitrogen for subsequent assays.

246

247 **Cells transfection**

248 RH30 and RH41 cells were transfected with 100nM of human DDX5 specific siRNA

249 (siDDX5 #1 and siDDX5 #2, Sigma-Aldrich) or scrambled control siRNA (siCTR) (siRNA

250 universal negative control, Sigma-Aldrich) using Lipofectamine 2000 (Invitrogen)

251 according to the manufacturer's protocol. Transfection with siRNAs was executed when

252 cultured cells reached a confluency of 60% in 6 well plates. Transfection was carried out

253 according to our adapted protocol in RPMI growth medium for 4-6 hours at 37°C.

254 Transfection was then stopped by removing the growth medium and replacing it with

255 RPMI with 10% fetal bovine serum. RNA or protein were isolated 72 h post-transfection

256 for all assays. The targeted sense and antisense strands are shown below:

257   siDDX5 #1

258   Sense: 5'-AACCGCAACCAUUGACGCCAU-3'

259   Antisense: 5'-AUGGCGUCAAUGGUUGCGGUU-3'

260   siDDX5 #2

261   Sense: 5'-GGCUAGAUGUGGAAGAUGU-3'

262   Antisense: 5'-ACAUCUUCCACAUCUAGCC-3'

263

264   **Short hairpin (sh)RNA lentivirus production and cell infections**

265   Lentiviruses were produced in HEK293T packaging cells seeded in 100 mm culture

266   dishes and transfected in 10ml of DMEM medium, using lipofectamine 2000 (Thermo

267   Fisher Scientific), with lentiviral packaging vectors psPAX2 (7 µg; Addgene) and pMD2.G

268   (3,5 µg; Addgene) and 10 µg lentiviral expression constructs shRNA pLKO.1-puro (G9a

269   Mission shRNA, Sigma-Aldrich, TRCN0000115671, NM_025256,); For DDX5

270   knockdown the custom sequence AACCGCAACCAUUGACGCCAU (Sigma-Aldrich

271   DDX5 Mission shRNA plasmid DNA, NM_004396.) was cloned in the pLKO.1-puro

272   vector. The non-silencing shCTR (mission control shRNA plasmid DNA) was purchased

273   from Sigma aldrich. Transfection medium was replaced 24 h later with new complete

274   DMEM and 48 h after transfection the lentiviral containing medium was collected, spun

275   to remove cell debris, and the supernatant filtered through a 0.45 µm low protein binding

276   filters. Viral aliquots immediately stored at -80°C. RH30 and RH41 target cells were

277   plated in a 100 mm dish (1,5x10^6 cells) and, 24 h later, were infected with lentiviral

278   pLKO.1-puro vectors expressing specific shRNA sequences for 24 h in the presence of

279   polybrene (8µg/ml; Sigma-Aldrich). After further 24 hrs, RH30 and RH41 cells were

280   selected with 1 µg/ml puromycin (Sigma-Aldrich, P8833) for 3 days. Cells were harvested

281   at different time points for subsequent experiments. All shRNAs were obtained from

282   Sigma Aldrich.

283

284   **In vitro proliferation assays**

285 Cells transfected with siRNA DDX5 and cells transduced with lentivirus shRNA G9a were

286 seeded in 6-well plates (1.8 10^5 cells per well) and cell proliferation was evaluated by

287 counting trypsinized cultures at 1, 2 and 3 days in RH30 and RH41 cells.

288

289 **RNA extraction and Quantitative real time PCR (qRT-PCR)**

290 Cells were harvested and centrifuged at 3000 rpm for 5 min at 4°C. Supernatant was

291 then removed and cell pellet was resuspended in 1 ml of ice-cold PBS and centrifuged

292 at 2000 rpm for 5 min at 4°C. After removing the supernatant, cell pellet was

293 resuspended in 1 mL of TRI Reagent (Sigma aldrich) and RNA extraction was carried

294 out following manufacturer's protocol. Quantity of RNA samples were assessed with

295 NanoDrop analysis (NanoDrop Technologies). cDNA synthesis was performed using a

296 High Capacity cDNA Reverse Transcription Kits (Applied Biosystems). qRT-PCR was

297 performed with a StepOne plus Real-Time PCR System (Applied Biosystems) to analyze

298 relative gene expression levels using SYBR Green Master mix (Applied Biosystems)

299 following manufacturer indications.

300 PCR amplification was performed as follows: 95°C 5 minutes, followed by 95°C for 10s,

301 annealing at 60°C for 10s, followed by 45 cycles at 72°C for 10s. Melting curves were

302 generated and tested for a single product after amplification. Expression of each target

303 was calculated using the 2-ΔΔCt method and expressed as a relative mRNA expression.

304 Relative expression values were normalized to the housekeeping gene GAPDH. qRT-

305 PCR was done using reaction duplicates and three independent biological replicates

306 were done for each analysis. Error bars indicate the mean ± standard deviation.

307 The primers we used are:

308 DDX5, For: 5'-GCCGGGACCGAGGGTTTGGT-3', Rev: 5'-

309 CTTGTGCTGTGCGCCTAGCCA-3'; AKT, For: 5'-TCTATGGCGCTGAGATTGTG-3',

310 Rev: 5'-CTTAATGTGCCCGTCCTTGT-3'; G9a For: 5'-AGAGTGTGGACGGAGAGCTC-

311 3' Rev: 5'-GGTCTCCCGCTTGAGGAT-3'; MyoD For: 5'-

13

312   CCGCCTGAGCAAAGTAAATGA-3'; Rev 5'-GCAACCGCTGGTTTGGATT-3'; RASSF4,

313   For: 5'-AGTCCATTCAGAAGTCGGAGC-3'; Rev: 5'-CCCCAGGCAATGTTGAGGAG-3';

314   PIPOX   For: 5'-GGAGCAGTTCTTTCTACCACAC-3';   Rev: 5'

315   TTCCCAGCAGCAGTAATCCA-3'; TFAP2B, For: 5'-TCAATGCATCTCTCCTCGGC-3';

316   Rev:5'-CAGCTTCTCCTTCCACCAGG-

317   3';MRAS,For:TGGCGACCAAACACAATATTCC; Rev: TCTCCCCGCCATTTGGTTTT-

318   3';ABAT,For:5'-CTGCCTCCGGAGAACTTTGT-3';Rev:5'-

319   TTTCCTTGCTCCGGTACCAC-3'; BMP5 For: AATGCCACCAACCACGCTAT Rev: 5'-

320   GCCACATGAGCGTACTACCA-3'; FGFR4, For: 5'-TGGCCGTCAAGATGCTCAAA-3';

321   Rev:5'-GTACAGGGGCCCTTCCTGG-3';GAPDHFor:5'-

322   TCTGGTAAAGTGGATATTGTTGCC-3';   Rev: 5'-CAAGCTTCCCGTTCTCAGCC-

323   3';PAX3-FOXO1,   For: 5'-AGACAGCTTTGTGCCTCCAT-3';   Rev: 5'-

324   CTCTTGCCTCCCTCTGGATT-3'; myogenin, For: 5'-TCAACCAGGAGGAGCGTGA-3ì;

325   Rev: 5'-TGTAGGGTCAGCCGTGAGCA-3'

326

327   **Protein extraction and Western blotting**

328   Cells were harvested and centrifuged at 3000 rpm for 5 min at 4°C. Supernatant was

329   then removed and cell pellet was resuspended in 1 ml of ice-cold PBS and centrifuged

330   at 2000 rpm for 5 min at 4°C. After removing the supernatant, cell pellet was

331   resuspended in lysis RIPA buffer supplemented with protease inhibitor cocktail and

332   phosphatase inhibitors (Roche) and incubated in ice for 30 min. Samples were then

333   sonicated in a water bath for 10 min (30 sec ON/ 30 sec OFF) and centrifuged at 15000

334   rpm for 15 min at 4°C. Supernatant was then transferred in a new tube and proteins were

335   quantified by BCA assay (Thermo Fisher Scientific) according to the manufacturer's

336   protocol. Cell lysates were resolved on 4%-20% Mini-PROTEAN TGX gels (Bio-Rad

337   Laboratories) and then transferred to nitrocellulose membrane (Amersham) using Trans-

338   Blot Turbo Transfer system (Bio-Rad Laboratories). Membranes were blocked with 5%

339   nonfat dried milk in Tris-buffered saline/Tween (TBS-T; 0.1%) for 1 hours at room

340   temperature with gentle shaking, followed by overnight incubation at 4°C with various

341   antibodies. The primary antibodies we used were: DDX5 (Cell Signalling, #9877), G9a

342   (Cell signalling, #3306), FOXO1 (Cell Signalling, #2880), p-AKT (Ser473) (Cell signaling,

343   #4058), AKT (Cell signaling #4685) PARP (Cell signaling #9542), cleaved caspase 7

344   (Cell signaling #8438), cleaved caspase 9 (Cell signaling #9505), MYOD (Santa Cruz

345   Biotechnology, C-20), myogenin (DSHB, F5D), GAPDH (Sigma, G9545), α-tubulin

346   (Sigma-Aldrich, T5168). Membranes were then incubated with HRP-conjugated

347   secondary antibodies (IgG-HRP Santa Cruz Biotechnologies) for 1 hour at RT and after

348   incubation the blots were developed in an ECL detection solution (Clarity Max ECL

349   substrate , Bio-Rad Laboratories) and signal was detected using ChemiDoc (BioRad

350   Laboratories).

351

352   **Mouse xenograft experiments**

353   All animal procedures were approved by Italian Ministry of Health and Istituto Superiore

354   di Sanità; approval number 7FF2C.7-EXT.9.

355   Female Balb/c nude mice (6/7 weeks old) were obtained from (Envigo) and maintained

356   under specific pathogen–free conditions in a temperature- and humidity-controlled

357   environment (Allevamenti Plaisant). 2×10^6 shCTR and shDDX5 RH30 cells were

358   injected subcutaneously into the flank of and, once tumors were palpable, they were

359   measured every other day by measuring 2 diameters (d1 and d2) in right angles using a

360   digital caliper. Total tumor volumes were then calculated by the formula $V = (4/3)\pi r3; r =$

361   (d1 + d2)/4. On day 21 after the injections, mice were euthanized and resected tumors

362   were fixed in formalin or immersed in liquid nitrogen and stored at -80 degrees. For

363   western analysis tumors were disrupted with a mortar and pestle, followed by sonication

15

364   in RIPA buffer supplemented with proteinase and phosphatase inhibitors (Roche).

365   Formalin-fixed tumor tissues were embedded in paraffin and and sections were stained

366   with hematoxylin and eosin using standard techniques (data not shown). Tissue sections

367   were deparaffinized, rehydrated, and heated at 95°C for 20 min in pH 6 antigen retrieval

368   buffer. Slides were blocked and incubated with Ki67 antibody (Abcam 15580) overnight

369   at 4°C, then incubated with the secondary antibody (Alexa Fluor 488, Thermo Fisher

370   Scientific). Nuclei were counterstained with DAPI (Sigma). Images were acquired using

371   Axio Observer 443 microscope (ZEISS) and analyzed by ZEN 3.0 (Blue edition)

372   software.

373

374   **Co-immunoprecipitation**

375   Co-immunoprecipitation was carried out through magnetic separation. RH30 and RH41

376   cells were centrifuged at 1200 rpm for 5 min at 4°C, resuspended in lysis buffer (10 mM

377   Tris pH 8, 10 mM NaCl, 0.1 mM EDTA pH 8, 0.1 mM EGTA) with protease inhibitor

378   (Roche) and then incubated on ice for 30 min. A dounce homogenizer was used to

379   mechanically help cell lysis. 10% NP-40 was added to a final concentration of 0,5% and

380   then samples were vortexed and incubated on ice 2-3 min. Samples were then

381   centrifuged at 4000 rpm for 5 min at 4°C in order to pellet nuclei. Nuclei were

382   resuspended in nuclei lysis buffer (20 mM Tris pH 8, 400 mM NaCl, 1 mM EDTA pH 8,

383   1 mM EGTA) with protease inhibitor (Roche) and incubated for 10 min on ice to increase

384   lysis efficiency. Lysates were then sonicated for 10 min (30 sec On/30 sec OFF at high

385   intensity) and then centrifuged at top speed for 20 min at 4°C. Supernatant, containing

386   nuclear extract (NE), was then transferred into a new tube: 50 μl on NE was saved to

387   use as input and to quantify NE concentration. NE was then precleared with 10 μl protein

388   A/G magnetic beads (Thermo Fisher Scientific), washed with IP lysis buffer (50 mM Tris

389   pH 8, 150 mM NaCl, 1 mM EDTA pH 8, 1 mM EGTA) for 2 hrs at 4°C on rotating wheel.

390 After preclearing, NE were diluted 1:5 in IP buffer with protease inhibitor (Roche). NE

391 was incubated overnight at 4°C on rotating wheel with 10 ug of G9a antibody (Abcam,

392 ab185050). The following day we added pre-blocked protein A/G magnetic beads

393 (Thermo Fisher Scientific) to each sample and incubated for 2 hrs at 4°C on rotating

394 wheel. Samples were then washed six times, one wash every 5 min, with IP buffer. At

395 the end, beads were separated on a magnet and the immunocomplexes were

396 resuspended with IP buffer and LSB buffer (Biorad Laboratories) for further analysis.

397

398 **RNA-Sequencing**

399 **RNAseq in siDDX5 FP-RMS**

400 Total RNA was extracted and quantified as previously described. RNA-Seq libraries

401 preparation and sequencing was performed by the IGA Technology Services (Udine,

402 Italy) using the Illumina TruSeq Stranded mRNA Kit (Illumina, San Diego, CA) according

403 to manufacturer's instructions. The final libraries for paired-end sequencing of 150 base

404 pairs were carried out on an Illumina NovaSeq6000 (Illumina, San Diego, CA) with an

405 average of 55 million of reads per sample. Processing raw data for both format

406 conversion and de-multiplexing were performed by *Bcl2Fastq* version 2.20 of the Illumina

407 pipeline. Reads quality was evaluated using *FastQC* (version 0.11.8, Babraham Institute

408 Cambridge, UK) tool, then adapter sequences were masked with *Cutadapt* version 1.11

409 from raw fastq data using the following parameters: *--anywhere* (on both adapter

410 sequences) *--overlap 5 --times 2 --minimum-length 35 --mask-adapter*.

411 Reads were mapped to the human Ensembl GRCh38 transcriptome index (release 96)

412 using *kallisto* (version 0.46.0) (28). The following flags were used for *kallisto*: *-b 30 --*

413 *bias*. Gene-level normalization and differential gene expression analysis were performed

414 using Bioconductor (29) R (version 3.6.2) (R Core Team, 2015) package *DESeq2*

415 version 1.26 (30) accounting for the presence of batch effects. The figures were obtained

17

416 using the *R* environment with package *ggplot2* version 3.3.0 and *pheatmap* version

417 1.0.12.

418

419 RNAseq in shG9a FP-RMS

420 RNA-seq libraries from total RNA (100 ng) from each sample were prepared using

421 QuantSeq 3'mRNA-Seq Library prep kit (Lexogen, Vienna, Austria) according to

422 manufacturer's instructions, at Telethon Institute of Genetics and Medicine (TIGEM). The

423 amplified fragmented cDNA of 300 bp in size were sequenced in single-end mode using

424 the NextSeq500 (Illumina) with a read length of 75 bp. Reads quality was evaluated

425 using *FastQC* (version 0.11.8, Babraham Institute Cambridge, UK) tool and was trimmed

426 using *TrimGalore* software to remove adapter and low-quality bases (Q < 20). Then

427 reads were mapped to the human Ensembl GRCh38 build reference genome using

428 *STAR* version 2.5.0a (31) using Gene annotations corresponding to the Ensembl

429 annotation release 96 which was used to build a transcriptome index and provided to

430 *STAR* during the alignment.

431 The same gene annotations were used to quantify the gene-level read counts using

432 *HTSeq-count* version 0.8.0 (32) script, subsequently the data normalization and

433 differential analysis for gene expression were performed using Bioconductor (29) R

434 package *edgeR* version 3.28 (33).

435

436 Gene set enrichment analysis

437 In order to understand biological meaning of the differentially expressed genes the

438 resulting filtered (Benjamini-Hochberg false discovery rate (FDR) adjusted for multiple

439 hypothesis testing p-value < 0.05) genes were clustered by functional annotation using

440 Bioconductor *R* package *clusterProfiler* version 3.14 (34) with annotation of Gene

441 Ontology Database (35) and with annotation of Kyoto Encyclopedia of Genes and

442 Genomes (KEGG) (36) for pathways. Gene Set Enrichment Analysis (GSEA) (37) with

443 pre-ranked, "classic" mode with 10,000 permutations was used to assess the enrichment

444 of the gene profile of siDDX5 or shG9a samples compared to control samples in the

445 curated "hallmark" and "C2" gene set collections (BROAD molecular signature database,

446 MSigDb version 6.2).

447

448 **Data availability**

449 RNA-Seq data accompanying this paper are available through NCBI's Gene Expression

450 Omnibus (GEO) repository, under accession number GSE152358 and GSE152359.

451

452 **Statistical analysis**

453 Data were analyzed using Prism (version 6.0; GraphPad Software Inc.), and images

454 were compiled in Photoshop (version 6.0; Adobe Systems). Results are presented as

455 mean ± SD from at least 3 independent experiments. Statistical analysis was conducted

456 using an unpaired Student's *t*-test, one-way ANOVA or 2-way ANOVA. *P* value of less

457 than 0.05 was considered statistically significant. *$P < 0.05$; **$P < 0.01$; ***$P < 0.001$;

458 ****$P < 0.0001$.

459

460 **Author Contributions**

461 A.G. performed all the experiments, collected and analysed data and prepared figures.

462 V.L. performed bioinformatic analyses. C.M. conceived, supervised the project and wrote

463 the manuscript. All authors discussed results, reviewed and edited the manuscript.

464

465 **Acknowledgements**

469   (core facilities, Bambino Gesù Children's Hospital, Rome, Italy) for the technical FFPE

470   tissues preparation.

471

472   **Declaration of Interests**

473   The authors declare no competing interests.

474   **References**

475   1.   Hettmer S, Li Z, Billin AN, Barr FG, Cornelison DD, Ehrlich AR, et al.
476   Rhabdomyosarcoma: current challenges and their implications for developing
477   therapies. *Cold Spring Harb Perspect Med.* 2014;4(11):a025650.

478   2.   El Demellawy D, McGowan-Jordan J, de Nanassy J, Chernetsova E, and Nasr A.
479   Update on molecular findings in rhabdomyosarcoma. *Pathology.*
480   2017;49(3):238-46.

481   3.   Wachtel M, and Schafer BW. PAX3-FOXO1: Zooming in on an "undruggable"
482   target. *Semin Cancer Biol.* 2018;50:115-23.

483   4.   Seki M, Nishimura R, Yoshida K, Shimamura T, Shiraishi Y, Sato Y, et al. Integrated
484   genetic and epigenetic analysis defines novel molecular subgroups in
485   rhabdomyosarcoma. *Nat Commun.* 2015;6:7557.

486   5.   Kohsaka S, Shukla N, Ameur N, Ito T, Ng CK, Wang L, et al. A recurrent
487   neomorphic mutation in MYOD1 defines a clinically aggressive subset of
488   embryonal rhabdomyosarcoma associated with PI3K-AKT pathway mutations.
489   *Nat Genet.* 2014;46(6):595-600.

490   6.   Shern JF, Chen L, Chmielecki J, Wei JS, Patidar R, Rosenberg M, et al.
491   Comprehensive genomic analysis of rhabdomyosarcoma reveals a landscape of
492   alterations affecting a common genetic axis in fusion-positive and fusion-
493   negative tumors. *Cancer Discov.* 2014;4(2):216-31.

494   7.   Gryder BE, Yohe ME, Chou HC, Zhang X, Marques J, Wachtel M, et al. PAX3-
495   FOXO1 Establishes Myogenic Super Enhancers and Confers BET Bromodomain
496   Vulnerability. *Cancer Discov.* 2017;7(8):884-99.

497   8.   Linder P, and Jankowsky E. From unwinding to clamping - the DEAD box RNA
498   helicase family. *Nat Rev Mol Cell Biol.* 2011;12(8):505-16.

499   9.   Caretti G, Schiltz RL, Dilworth FJ, Di Padova M, Zhao P, Ogryzko V, et al. The RNA
500   helicases p68/p72 and the noncoding RNA SRA are coregulators of MyoD and
501   skeletal muscle differentiation. *Dev Cell.* 2006;11(4):547-60.

502   10.   Dardenne E, Polay Espinoza M, Fattet L, Germann S, Lambert MP, Neil H, et al.
503   RNA helicases DDX5 and DDX17 dynamically orchestrate transcription, miRNA,
504   and splicing programs in cell differentiation. *Cell Rep.* 2014;7(6):1900-13.

505   11.   Yang L, Lin C, and Liu ZR. Phosphorylations of DEAD box p68 RNA helicase are
506   associated with cancer development and cell proliferation. *Mol Cancer Res.*
507   2005;3(6):355-63.

508   12.   Shin S, Rossow KL, Grande JP, and Janknecht R. Involvement of RNA helicases
509   p68 and p72 in colon cancer. *Cancer Res.* 2007;67(16):7572-8.

510 13. Nyamao RM, Wu J, Yu L, Xiao X, and Zhang FM. Roles of DDX5 in the
511   tumorigenesis, proliferation, differentiation, metastasis and pathway regulation
512   of human malignancies. *Biochim Biophys Acta Rev Cancer.* 2019;1871(1):85-98.
513 14. Stewart E, McEvoy J, Wang H, Chen X, Honnell V, Ocarz M, et al. Identification of
514   Therapeutic Targets in Rhabdomyosarcoma through Integrated Genomic,
515   Epigenomic, and Proteomic Analyses. *Cancer Cell.* 2018;34(3):411-26 e19.
516 15. Ernst J, and Kellis M. ChromHMM: automating chromatin-state discovery and
517   characterization. *Nat Methods.* 2012;9(3):215-6.
518 16. Skapek SX, Ferrari A, Gupta AA, Lupo PJ, Butler E, Shipley J, et al.
519   Rhabdomyosarcoma. *Nat Rev Dis Primers.* 2019;5(1):1.
520 17. Cox AD, Fesik SW, Kimmelman AC, Luo J, and Der CJ. Drugging the undruggable
521   RAS: Mission possible? *Nat Rev Drug Discov.* 2014;13(11):828-51.
522 18. Yohe ME, Gryder BE, Shern JF, Song YK, Chou HC, Sindiri S, et al. MEK inhibition
523   induces   MYOG   and   remodels   super-enhancers   in   RAS-driven
524   rhabdomyosarcoma. *Sci Transl Med.* 2018;10(448).
525 19. Laplante M, and Sabatini DM. mTOR signaling in growth control and disease. *Cell.*
526   2012;149(2):274-93.
527 20. Zhang X, Tang N, Hadden TJ, and Rishi AK. Akt, FoxO and regulation of apoptosis.
528   *Biochim Biophys Acta.* 2011;1813(11):1978-86.
529 21. Xue Y, Jia X, Li L, Dong X, Ling J, Yuan J, et al. DDX5 promotes hepatocellular
530   carcinoma tumorigenesis via Akt signaling pathway. *Biochem Biophys Res
531   Commun.* 2018;503(4):2885-91.
532 22. Bhat AV, Palanichamy Kala M, Rao VK, Pignata L, Lim HJ, Suriyamurthy S, et al.
533   Epigenetic Regulation of the PTEN-AKT-RAC1 Axis by G9a Is Critical for Tumor
534   Growth in Alveolar Rhabdomyosarcoma. *Cancer Res.* 2019;79(9):2232-43.
535 23. Legrand JMD, Chan AL, La HM, Rossello FJ, Anko ML, Fuller-Pace FV, et al. DDX5
536   plays essential transcriptional and post-transcriptional roles in the maintenance
537   and function of spermatogonia. *Nat Commun.* 2019;10(1):2278.
538 24. Fiszbein A, Giono LE, Quaglino A, Berardino BG, Sigaut L, von Bilderling C, et al.
539   Alternative Splicing of G9a Regulates Neuronal Differentiation. *Cell Rep.*
540   2016;14(12):2797-808.
541 25. Cornett EM, Ferry L, Defossez PA, and Rothbart SB. Lysine Methylation
542   Regulators Moonlighting outside the Epigenome. *Mol Cell.* 2019;75(6):1092-101.
543 26. Ren YX, Finckenstein FG, Abdueva DA, Shahbazian V, Chung B, Weinberg KI, et
544   al. Mouse mesenchymal stem cells expressing PAX-FKHR form alveolar
545   rhabdomyosarcomas by cooperating with secondary mutations. *Cancer Res.*
546   2008;68(16):6587-97.
547 27. Davicioni E, Finckenstein FG, Shahbazian V, Buckley JD, Triche TJ, and Anderson
548   MJ. Identification of a PAX-FKHR gene expression signature that defines
549   molecular   classes   and   determines   the   prognosis   of   alveolar
550   rhabdomyosarcomas. *Cancer Res.* 2006;66(14):6936-46.
551 28. Bray NL, Pimentel H, Melsted P, and Pachter L. Near-optimal probabilistic RNA-
552   seq quantification. *Nat Biotechnol.* 2016;34(5):525-7.
553 29. Gentleman RC, Carey VJ, Bates DM, Bolstad B, Dettling M, Dudoit S, et al.
554   Bioconductor: open software development for computational biology and
555   bioinformatics. *Genome Biol.* 2004;5(10):R80.

556 30. Love MI, Huber W, and Anders S. Moderated estimation of fold change and
557   dispersion for RNA-seq data with DESeq2. *Genome Biol.* 2014;15(12):550.
558 31. Dobin A, Davis CA, Schlesinger F, Drenkow J, Zaleski C, Jha S, et al. STAR: ultrafast
559   universal RNA-seq aligner. *Bioinformatics.* 2013;29(1):15-21.
560 32. Anders S, Pyl PT, and Huber W. HTSeq--a Python framework to work with high-
561   throughput sequencing data. *Bioinformatics.* 2015;31(2):166-9.
562 33. Robinson MD, McCarthy DJ, and Smyth GK. edgeR: a Bioconductor package for
563   differential expression analysis of digital gene expression data. *Bioinformatics.*
564   2010;26(1):139-40.
565 34. Yu G, Wang LG, Han Y, and He QY. clusterProfiler: an R package for comparing
566   biological themes among gene clusters. *OMICS.* 2012;16(5):284-7.
567 35. Ashburner M, Ball CA, Blake JA, Botstein D, Butler H, Cherry JM, et al. Gene
568   ontology: tool for the unification of biology. The Gene Ontology Consortium. *Nat
569   Genet.* 2000;25(1):25-9.
570 36. Ogata H, Goto S, Sato K, Fujibuchi W, Bono H, and Kanehisa M. KEGG: Kyoto
571   Encyclopedia of Genes and Genomes. *Nucleic Acids Res.* 1999;27(1):29-34.
572 37. Subramanian A, Tamayo P, Mootha VK, Mukherjee S, Ebert BL, Gillette MA, et al.
573   Gene set enrichment analysis: a knowledge-based approach for interpreting
574   genome-wide expression profiles. *Proc Natl Acad Sci U S A.* 2005;102(43):15545-
575   50.

576

577
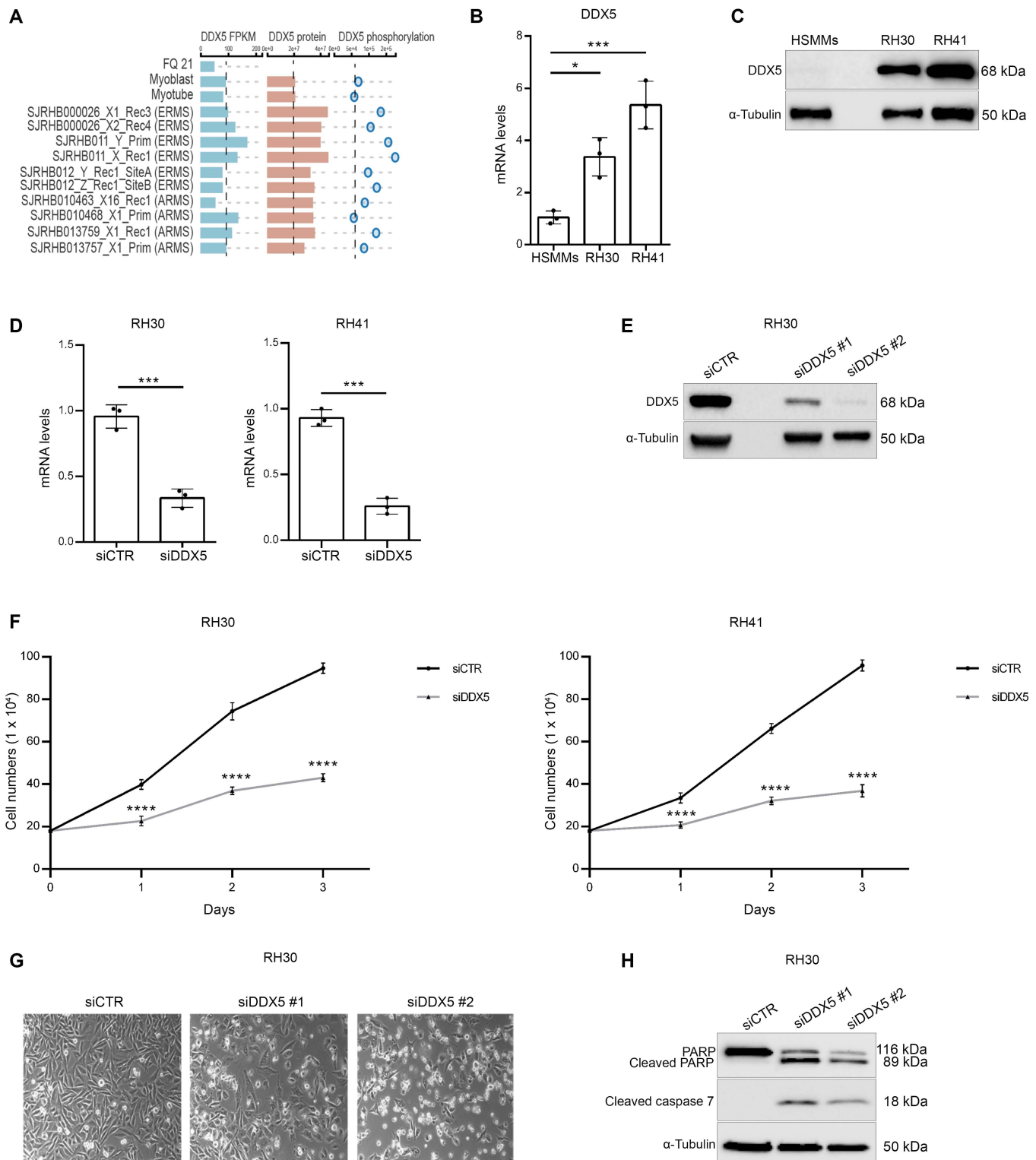
FIGURE 1

Figure 1. DDX5 is overexpressed in alveolar rhabdomyosarcoma and promotes FP-ARMS survival
(**A**) RNA (FPKM; blue bars) and protein levels (red bars), together with phosphorylation status (blue circles) of DDX5 in orhtotipic RMS patient-derived xenografts (PDX), as compared to normal myoblasts and myotubes. Data derive from https://pecan.stjude.cloud/proteinpaint/study/RHB2018 (14).
(**B**) Histogram showing the relative mRNA expression levels of DDX5 in RH30 and RH41 cell lines and human skeletal muscle myoblasts (HSMMs). Transcription values were assessed by qRT-PCR and normalized to GAPDH. Graph represents mean +/- SD from n=3 independent experiments.
(**C**) Representative western blot analysis for DDX5 in RH30 and RH41 cell lines and HSMMs. α-tubulin was used as a loading control.
(**D**) **q**RT-PCR analysis of DDX5 mRNA levels in RH30 (left) and RH41 (right) cell lines, after siCTR and siDDX5 treatment. Graphs show mean +/- SD from n=3 independent experiments. (**E**) Western blot analysis for DDX5 in RH30 cells treated with siCTR, and two different sequences for DDX5 (siDDX5 #1 and #2). Normalization with α-tubulin. (**F**) Cells growth curves after siDDX5 treatment. Cells were counted 1, 2 and 3 days after treatment. Graphs show mean +/- SD from n=3 independent experiments. (**G**) Representative phase contrast images of RH30 cells 3 days after siDDX5 treatment. (**H**) Western blot analysis for indicated proteins performed on RH30 after siDDX5 and siCTR treatment. α-tubulin was used as control of loading normalization. Statistical significance has been assessed in (**B**) by one-way ANOVA with Bonferroni multiple comparisons test. * p < 0.05; ***p < 0.001; (**D**) by an unpaired Student's t-test; *** p < 0.001; and (**F**) with 2-way anova with Sidak's multiple comparison test, .***p < 0.001 test.
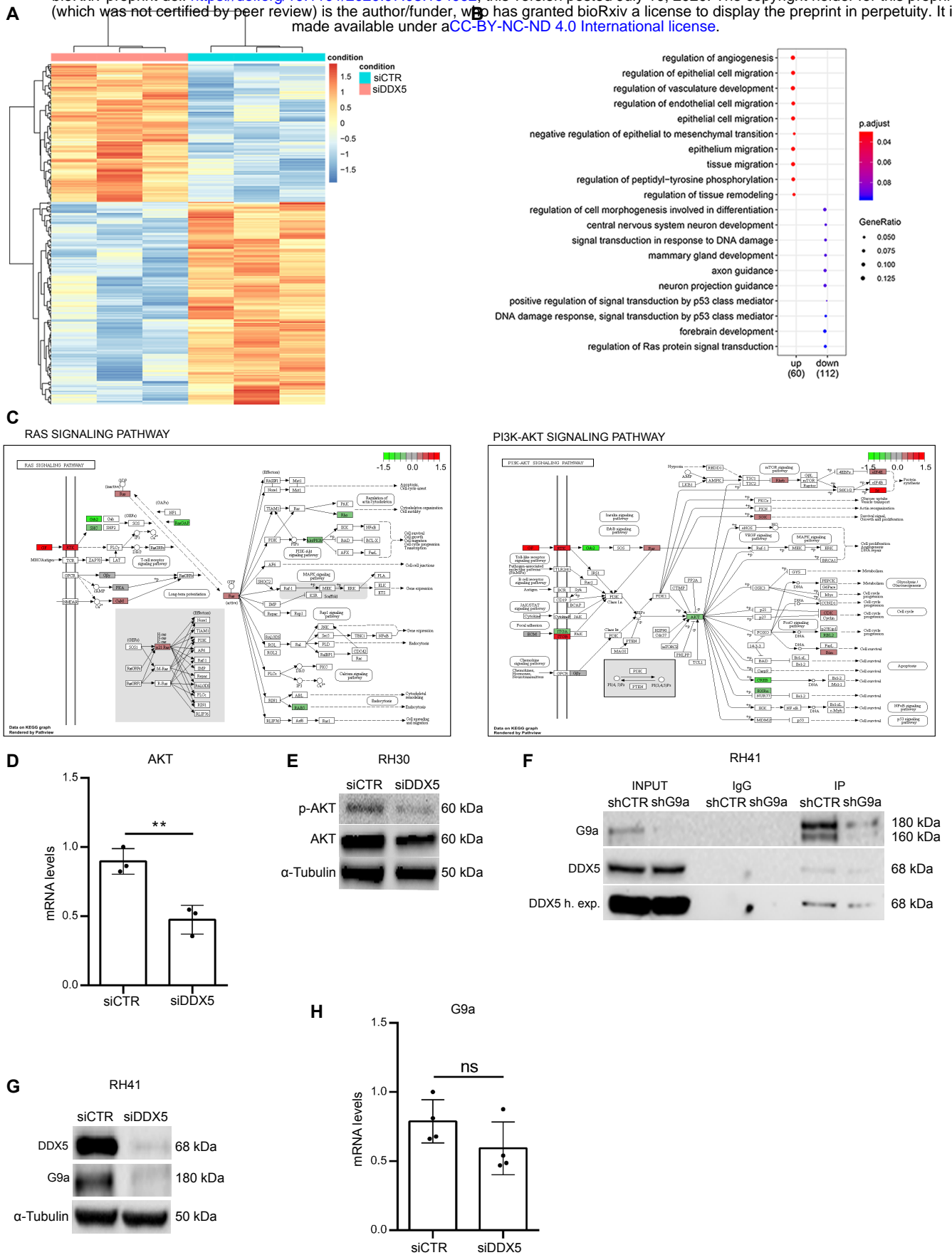
FIGURE 2

Figure 2 DDX5 interacts with G9a and regulates G9a-AKT signaling

(**A**) Heatmap plot of hierarchical clustering of all differentially expressed genes (DEGs). The X axis represents the two compared samples (siCTR and siDDX5). The Y axis represents DEGs. The color (from blue to red) represents gene expression intensity from low to high. Red indicates upregulated and blue represents downregulated genes. DEGs were selected according to FC > 1,5 e padj < 0.05. (**B**) Dot plot showing the up and down regulated GO terms of biological processes identified. The size of the dot is based on gene count enriched in the pathway, and the color of the dot shows the pathway enrichment significance. (**C**) KEGG analysis of Ras (left) and PI3K-AKT (right) signaling pathways.(**D**) AKT mRNA levels quantified by qRT-PCR after DDX5 silencing in RH30 cells, as compared to siCTR cells. Transcription values were assessed by qRT-PCR and normalized to GAPDH. Graph represents mean +/- SD from n=3 independent experiments. Statistical significance assessed by unpaired Student's t-test;** p <0.01). (**E**) Western blot analysis of p-AKT and AKT in siCTR and siDDX5 RH30 cells. Normalization with α-tubulin (**F**) Representative western blot analysis of the indicated proteins in G9a immunoprecipitation in nuclear extracts of control (shCTR) and shG9a-treated RH41 cells (last two right lanes). Equal amounts of nuclear extracts were immunoprecipitated with IgG as negative control. Inputs are shown on the left. (**G**) Western blot analysis for G9a and DDX5 in RH30 cells treated with siCTR and siDDX5. α-tubulin was used as loading control. (**H**) qRT-PCR for G9a in siCTR and siDDX5 RH30 cells. Graph shows the mean +/- SD value derived from n=4 independent experiments. Statistical significance has been assessed by an unpaired Student's t-test; p > 0,05 (no statistical significance, ns).
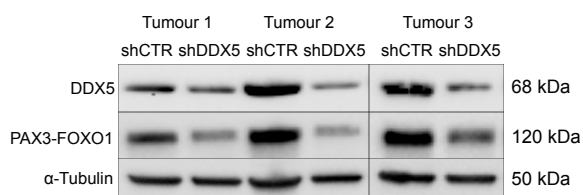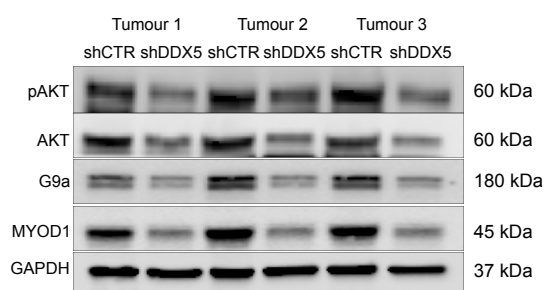
FIGURE 3
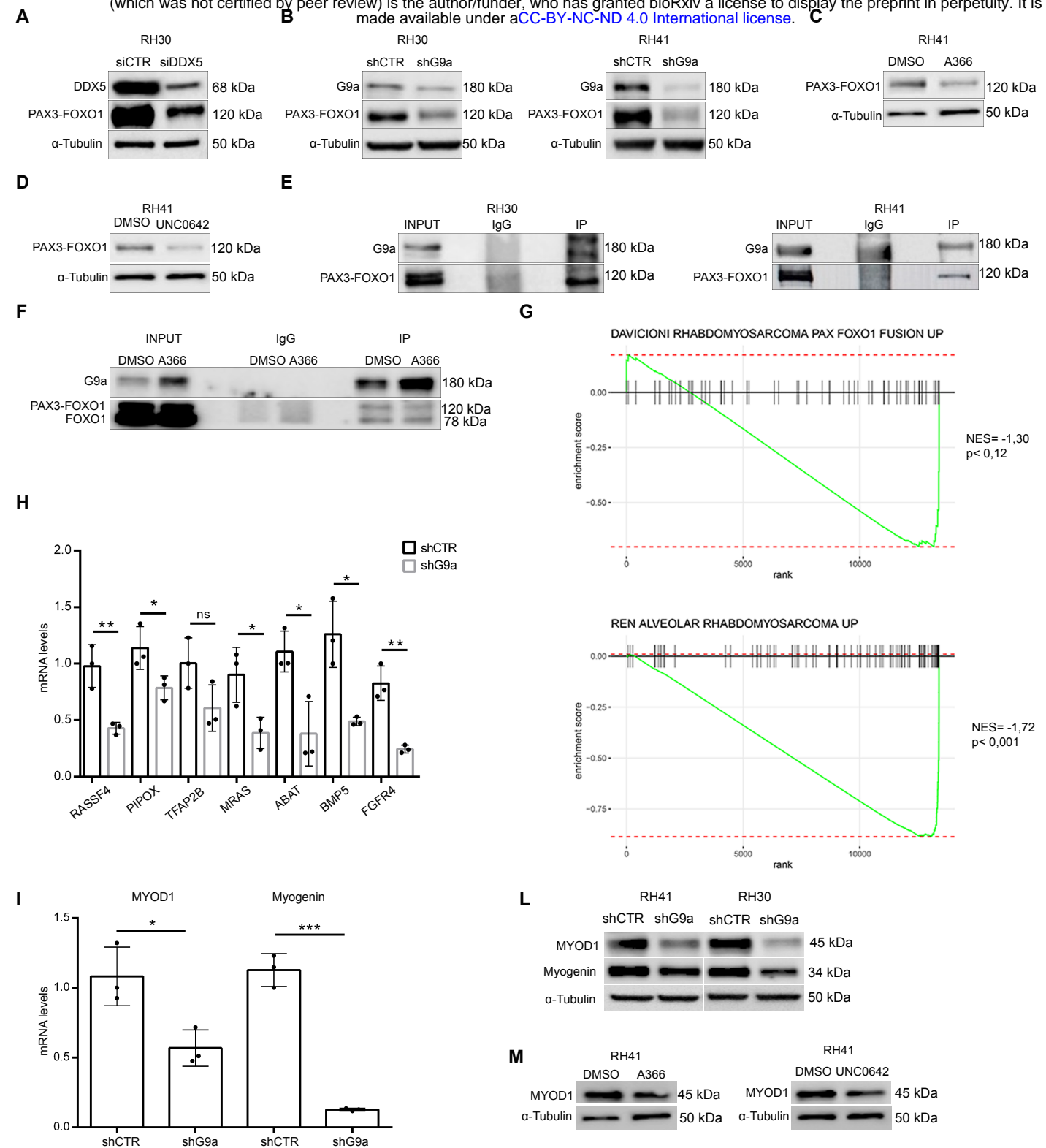
Figure 3
DDX5 and G9a regulate PAX3-FOXO1 expression

(**A**) Western blot analysis for DDX5 and PAX3-FOXO1 in RH30 cells treated with siCTR and siDDX5. α-Tubulin shown as loading control. (**B**) Western blot for G9a and PAX3-FOXO1 in RH30 (left) and RH41 (right) cells treated with shCTR and shG9a. α-Tubulin shown as loading control. (**C-D**) Western blot for PAX3-FOXO1 in RH41 cells treated with 10μM A366 (**C**) and 2 μM UNC0642 (**D**) for six days. Control cells were treated with DMSO and all samples were normalized with α-Tubulin. (**E**) Western blot analysis of G9a immunoprecipitation in RH30 (left) and RH41 (right) cells. PAX3-FOXO1 is detected in the G9a immunoprecipitates, but not in the IgG negative control. Input are shown on the left. (**F**) Western blot analysis for G9a and PAX3-FOXO1 in RH41 cells treated with A-366 as indicated in (**C**) and immunoprecipitated for G9a. IgG were used as a negative control. (**G**) GSEA of RNA-seq performed in shCTR and shG9a RH41 cells , on genes found upregulated by PAX3-FOXO1, using two different data sets (27) and (26). (**H**) Validation of the indicated PAX3-FOXO1 target genes by qRT-PCR in shCTR and shG9a cells. Transcription values were normalized to GAPDH. Graphs show the mean +/- SD from n=3 independent experiments. (**I**) mRNA levels of MYOD1 and myogenin quantified by qRT-PCR after shG9a treatment in RH41 and RH30 cells. Transcription values were normalized to GAPDH. Graphs show the mean +/- SD from n=3 independent experiments. (**L**) Western blot analysis for MYOD1 and Myogenin in RH41 and RH30 cells after shCTR and shG9a. α-tubulin was used for normalization. (**M**) Western blot of MYOD and MYOG protein levels in RH41 cells treated with 10 μM A366 or with 2 μM UNC0642 for six days. α-tubulin was used for normalization. Statistical significance has been assessed in (**H**) and (**I**) by unpaired Student's t-test; (* p < 0.05, ** p < 0.01, *** p < 0.001, ns > 0.05).

FIGURE 4
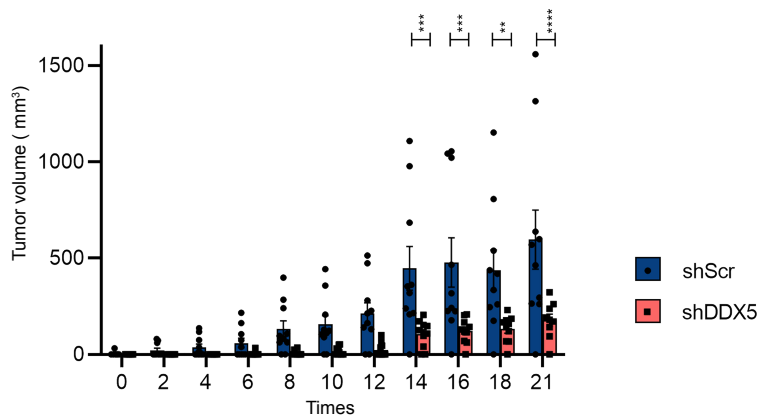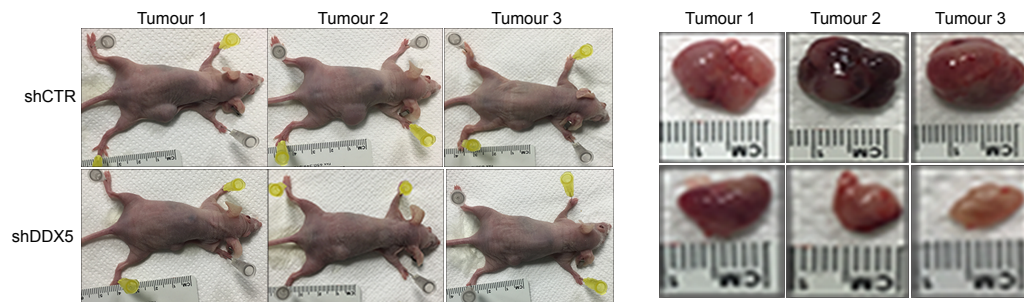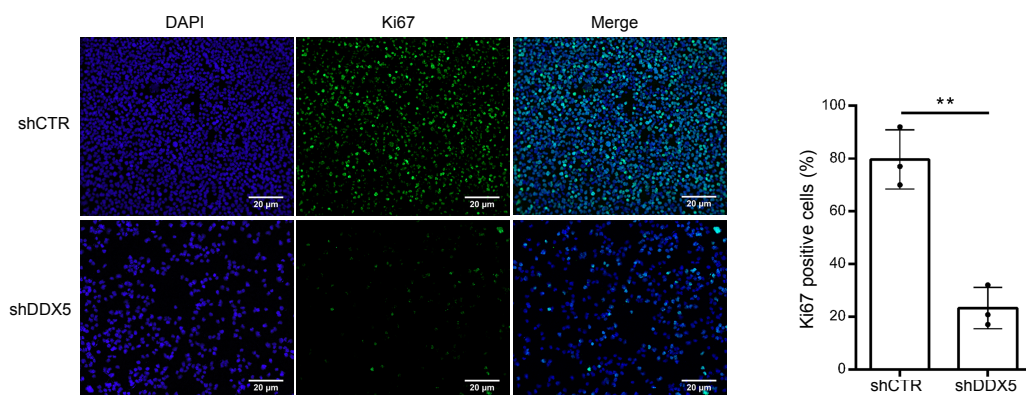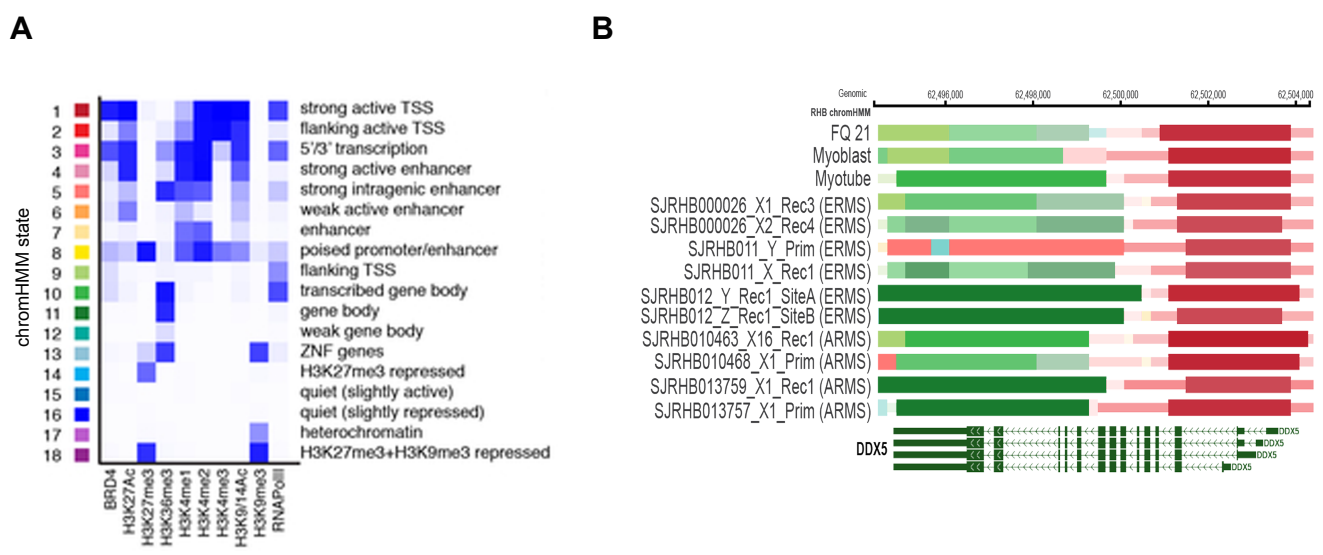
Figure 4
DDX5 promotes FP-RMS growth in vivo.
(**A**) Bar charts represent tumor volumes in sCTR and shDDX5 treated mice from day of injection (day 0) to day of tumor resection (day 21). Data are presented as mean +/-sem of n=10 mice/experimental group. Statistical significance assessed by 2-way Anova, with Sidak's multiple comparison test. ** p<0.01, *** p<0.001, **** p<0.0001. (**B**) Three representative shCTR and shDDX5 treated mice and matching resected tumors at day 21. (**C**) Representative images of Ki67 immunostaining (green) on isolated shCTR and shDDX5 tumors. DAPI (blue) was used to stain nuclei. Scale bars: 20 µm. Histogram (on the right) shows quantification of the percentage of Ki67+ cells. Data are represented as mean +/- sd of n=3 independent tumors. (**D-E**) Western blot analysis for the indicated protein on extracts derived from n=3 tumors/experimental group. α-tubulin and GAPDH were used for normalization.

Supplemental Figure 1

Supplemental Figure 1
(**A**) Legend of the 18 chromatin hidden Markov modeling (chromHMM) states (15) identified in the study (14). (**B**) ChromHMM state of DDX5 in RMS patient-derived xenografts (PDX) from ERMS and ARMS, as compared to normal myoblasts and myotubes. The bars show a strong active transcription start site (TSS) (red bars) and an actively transcribed gene body (green bars) in either normal myoblasts and myotubes, and primary ERMS and ARMS samples.

Supplemental Figure 2

A

B

C
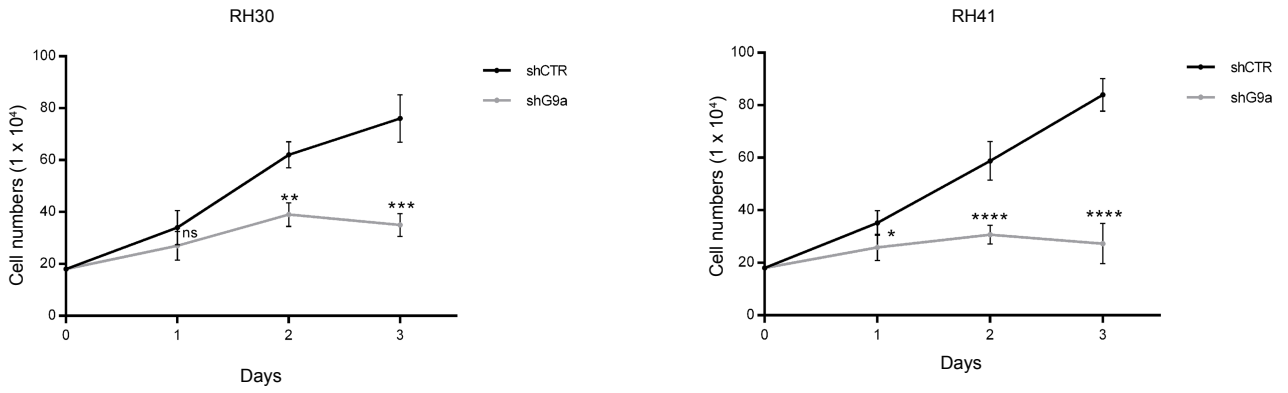
Supplemental Figure 2
(**A**) RH30 and RH41 cells growth curves after shCTR and shG9a treatment. Cells were counted 1, 2 and 3 days after treatment. Graphs show mean +/- SD from n=3 independent experiments Statistical significance has been assessed by 2-way Anova, with Sidak's multiple comparison test. ** $p<0.01$, *** $p<0.001$, **** $p<0.0001$. (**B**) Representative phase contrast images of RH30 (left) and RH41 (right), shCTR and shG9a, analyzed after 3 days after treatment. (**C**) Western blot of G9a, cleaved PARP, cleaved caspase 7 and cleaved caspase 9 from extracts of RH30 and RH41 cells 3 days after shG9a silencing. Normalization with α-tubulin.
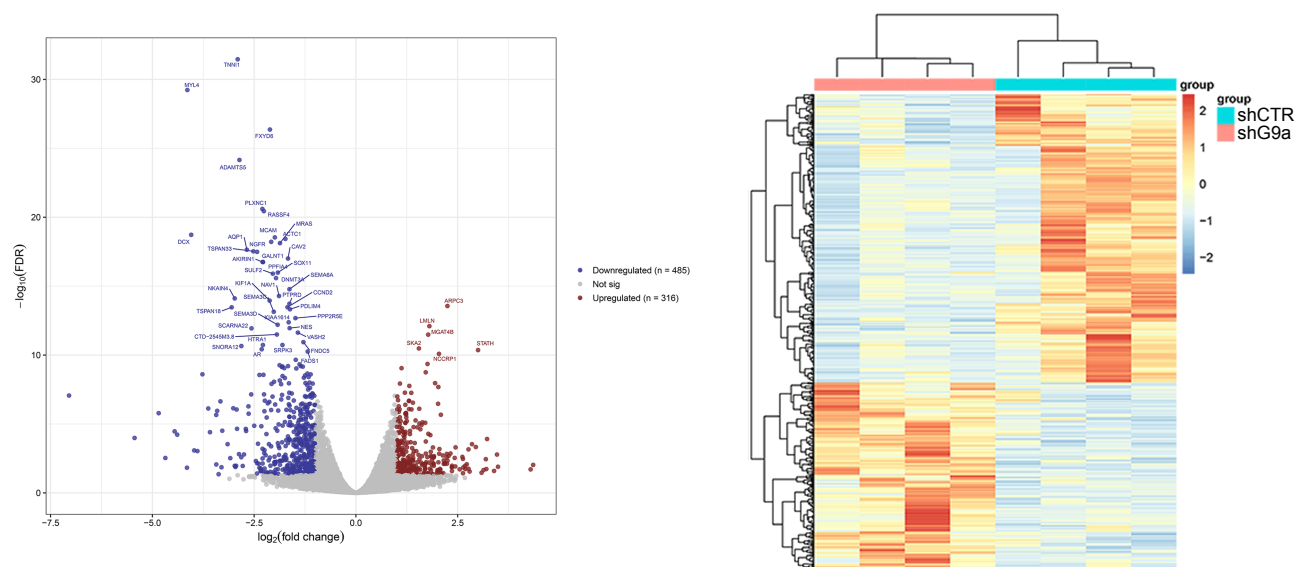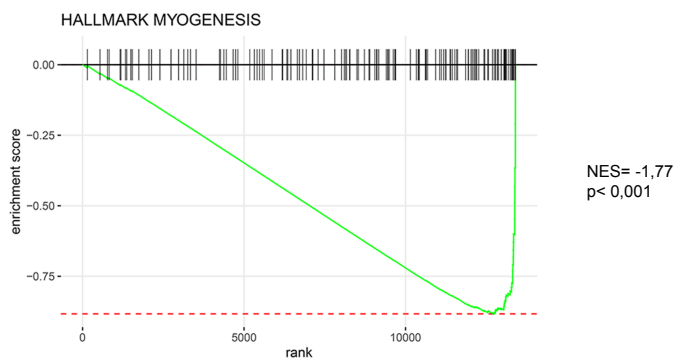
Supplemental Figure 3

A

B

C
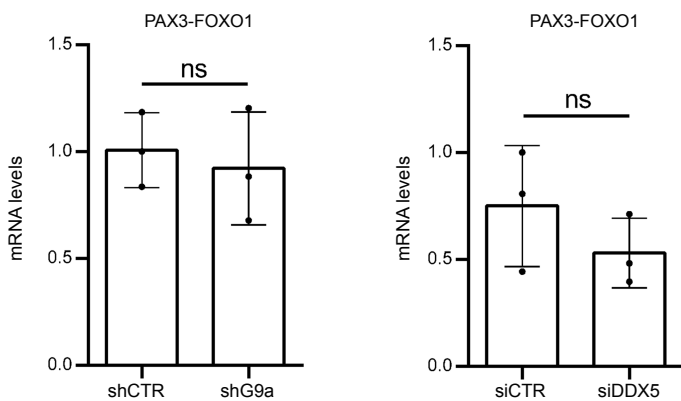
Supplemental Figure 3

(**A**) qRT-PCR of PAX3-FOXO1 in shG9a and siDDX5 treatments. Graphs show the mean +/-SD values from n=3 independent experiments. Statistical significance has been assessed by an unpaired Student's t-test; p > 0,05 (no statistical significance, ns). (**B**) RNA-seq analysis after G9a knockdown. Volcano plot of shG9a vs shCTR in RH41 cells (left) showing differentially expressed genes (DEGs) (downregulated genes are highlighted in blue and upregulated genes are red). Heatmap of DEGs in RH41 cells 72h after transfection (right). RNAseq analysis was performed for genes that are regulated by G9a at the transcript-level with more than two-fold regulation (Foldchange > 2 and FDR < 0.05). (**C**) GSEA of RNA-seq performed in shCTR and shG9a RH41 cells, on "Myogenesis" signature.